

## Supplementary Information

### **Enhanced spin pumping into superconductors provides evidence for superconducting pure spin currents**

Kun-Rok Jeon,<sup>1,2</sup> Chiara Ciccarelli,<sup>2\*</sup> Andrew J. Ferguson,<sup>2</sup> Hidekazu Kurebayashi,<sup>3</sup>

Lesley F. Cohen,<sup>4</sup> Xavier Montiel,<sup>5</sup> Matthias Eschrig,<sup>5</sup>

Jason W. A. Robinson,<sup>1</sup> and Mark G. Blamire<sup>1\*</sup>

<sup>1</sup>*Department of Materials Science and Metallurgy, University of Cambridge, 27 Charles Babbage Road, Cambridge CB3 0FS, UK*

<sup>2</sup>*Cavendish Laboratory, University of Cambridge, Cambridge CB3 0HE, UK*

<sup>3</sup>*London Centre for Nanotechnology and Department of Electronic and Electrical Engineering at University of College London, London WC1H 0IH, UK*

<sup>4</sup>*The Blackett Laboratory, Imperial College London, SW7 2AZ, UK*

<sup>5</sup>*Department of Physics, Royal Holloway, University of London, Egham Hill, Egham, Surrey TW20 0EX, UK*

\*To whom correspondence should be addressed: [cc538@cam.ac.uk](mailto:cc538@cam.ac.uk), [mb52@cam.ac.uk](mailto:mb52@cam.ac.uk)

#### **This PDF file includes:**

Supplementary Text

Figs. S1 to S12

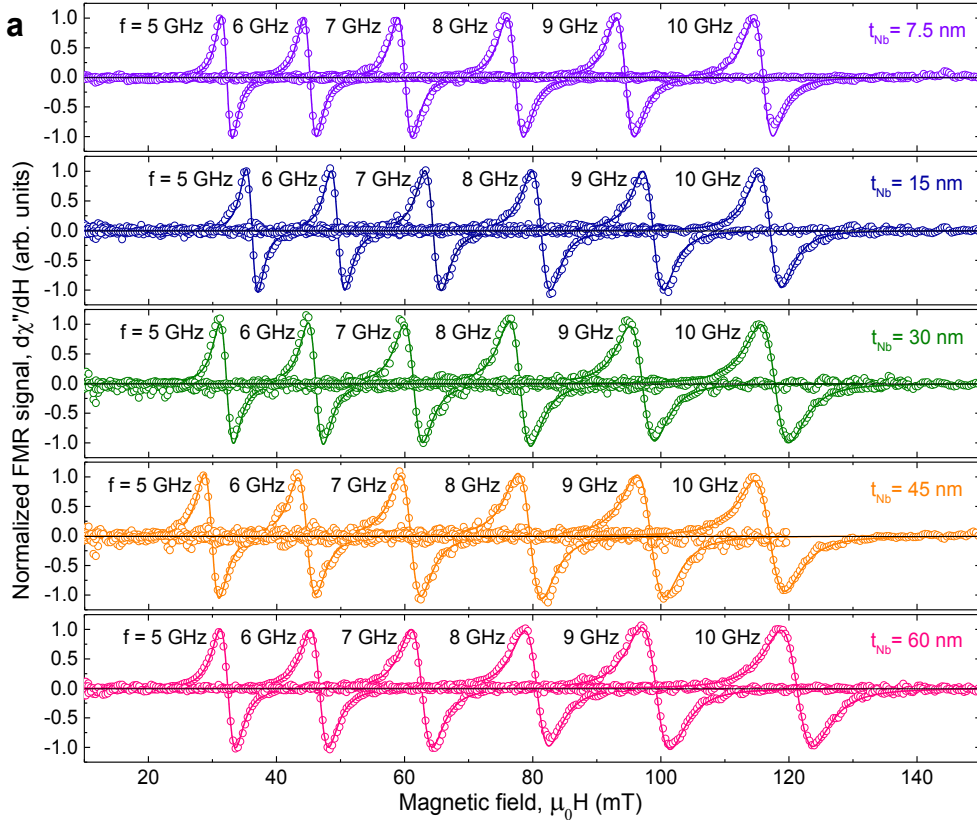
References (S1-S13)

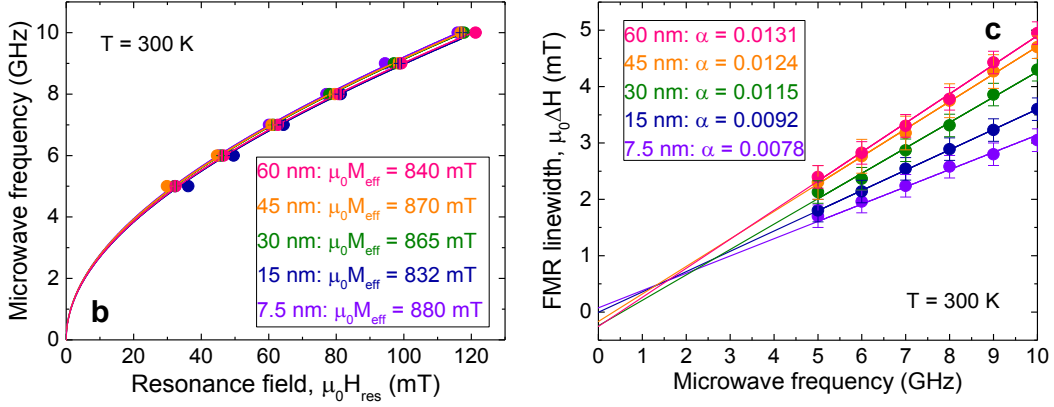
**Section S1. MW frequency dependence of FMR spectra for Nb/Ni<sub>80</sub>Fe<sub>20</sub>/Nb samples at room temperature.**

Figure S1 displays the set of FMR spectra attained from the samples without Pt layers at 300 K, from which the data shown in the inset of Fig. 2b (main text) were extracted. Note that to accurately determine the resonance magnetic field  $\mu_0 H_{res}$  and the FMR (peak-to-peak) linewidth  $\mu_0 \Delta H$ , we fitted all the data presented with the field derivative of Lorentzian function<sup>S1</sup> as follows:

$$\frac{d\chi''}{dH} \propto \frac{(\Delta H_{HWHM})^2 \cdot (H - H_{res})}{[(\Delta H_{HWHM})^2 + (H - H_{res})^2]^2} \quad (S1)$$

where  $\mu_0 H$  is the external (DC) magnetic field and  $\mu_0 \Delta H_{HWHM} = \frac{\sqrt{3}}{2} \mu_0 \Delta H$  is the half-width-at-half-maximum (HWHM) of the imaginary part  $\chi''$  of the magnetic susceptibility.





**Figure S1. a**, MW frequency dependence of FMR spectra for the Nb/Ni<sub>80</sub>Fe<sub>20</sub>/Nb samples at 300 K. The open symbols represent experimental data whereas the solid lines are fits with the field derivative of Lorentzian function [Eq. (S1)]. **b**, Microwave frequency vs. resonance magnetic field  $\mu_0 H_{\text{res}}$ . The solid lines are fits to estimate the effective saturation magnetization  $\mu_0 M_{\text{eff}}$  via Kittel's formula [Eq. (S2)]. **c**, FMR linewidth  $\mu_0 \Delta H$  as a function of microwave frequency. The solid lines are fitting curves to deduce the Gilbert damping constant  $\alpha$  using Eq. (S3). Error bars denote standard deviation of multiple measurements.

The MW frequency  $f$  dependences of  $\mu_0 H_{\text{res}}$  and  $\mu_0 \Delta H$  for each Nb thickness are respectively summarized in Figs. S1b and S1c. The dispersion relation of  $\mu_0 H_{\text{res}}$  with  $f$  is given by Kittel's formula:

$$f = \frac{\gamma}{2\pi} \sqrt{[\mu_0 (H_{\text{res}} + M_{\text{eff}}) \cdot \mu_0 H_{\text{res}}]}, \quad (\text{S2})$$

where  $\gamma = g_L \mu_B / \hbar$  is the gyromagnetic ratio ( $1.84 \times 10^{11} \text{ T}^{-1} \text{ s}^{-1}$ ),  $g_L$  is the Landé g-factor (taken to be 2.1)<sup>S2</sup>,  $\mu_B$  is the Bohr magneton, and  $\hbar$  is Plank's constant divided by  $2\pi$ . The values of  $\mu_0 M_{\text{eff}}$  determined from Fig. S1b using Eq. (S2) are in the range of 832 – 880 mT, fairly consistent with those for sputter-grown Ni<sub>80</sub>Fe<sub>20</sub> films<sup>S3</sup>. In Fig. S1c where  $\mu_0 \Delta H$  scales linearly with  $f$  for all cases, we can calculate the Gilbert-type damping constant  $\alpha$  using the following equation:

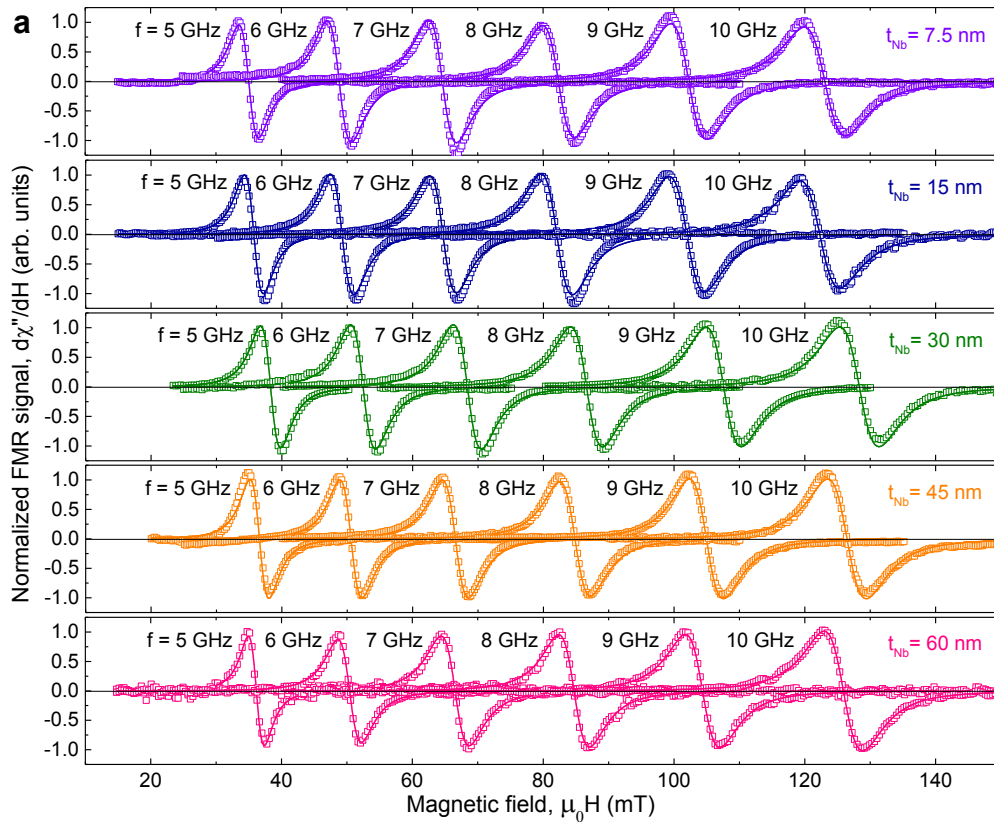
$$\mu_0 \Delta H(f) = \mu_0 \Delta H_0 + \frac{4\pi\alpha f}{\sqrt{3}\gamma} \quad (\text{S3})$$

with  $\mu_0 \Delta H_0$  is the zero-frequency line broadening due to long-range magnetic

inhomogeneities<sup>S4</sup> in the FM. All of the samples have small  $\mu_0\Delta H \leq |0.3 \text{ mT}|$ , meaning the high quality of the samples and the absence of two-magnon scattering. We note the clear enhancement of  $\alpha$  with  $t_{\text{Nb}}$  from  $7.8 \times 10^{-3}$  to  $13.1 \times 10^{-3}$  (Fig. S1c), which is the indicative of spin absorption/dissipation in the Nb layers by the spin pumping<sup>3,4,S5-S7</sup>.

## **Section S2. MW frequency dependence of FMR spectra for Pt/Nb/Ni<sub>80</sub>Fe<sub>20</sub>/Nb/Pt samples at room temperature.**

In this section, we present the set of FMR spectra obtained from the samples with Pt layers at 300 K (Fig. S2a), from which the data exhibited in the inset of Fig. 2D (main text) were extracted. It can be seen in Fig. S2c that Gilbert damping constant  $\alpha$  gradually decreases as the Nb thickness  $t_{\text{Nb}}$  increases even though the dependence of  $\alpha$  on  $t_{\text{Nb}}$  is much weaker than that for the samples without Pt layers (see Fig. S1c). The zero-frequency line broadening  $\mu_0\Delta H_0$  was also found to be less than  $|0.5 \text{ mT}|$ , which was ignorable small for the high  $f$  regime ( $\geq 10 \text{ GHz}$ ).



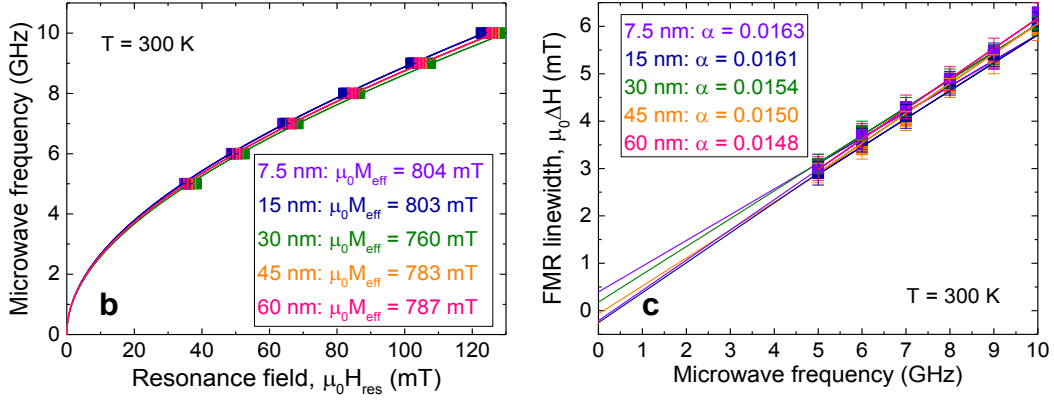


**Figure S2. MW frequency dependence of FMR spectra for the Pt/Nb/Ni<sub>80</sub>Fe<sub>20</sub>/Nb/Pt samples at 300 K.** a-c, The data shown are similar to those in Fig. S1 but now for the samples with Pt layers. Error bars denote standard deviation of multiple measurements.

Note that to minimize the contribution of  $\mu_0\Delta H_0$  to the (total) FMR linewidth  $\mu_0\Delta H(f)$  [see Eq. (S3)], a higher  $f$  of 20 GHz was used especially for low- $T$  FMR measurements.

### **Section S3. Estimation of the spin transport parameters for Nb/Ni<sub>80</sub>Fe<sub>20</sub>/Nb samples.**

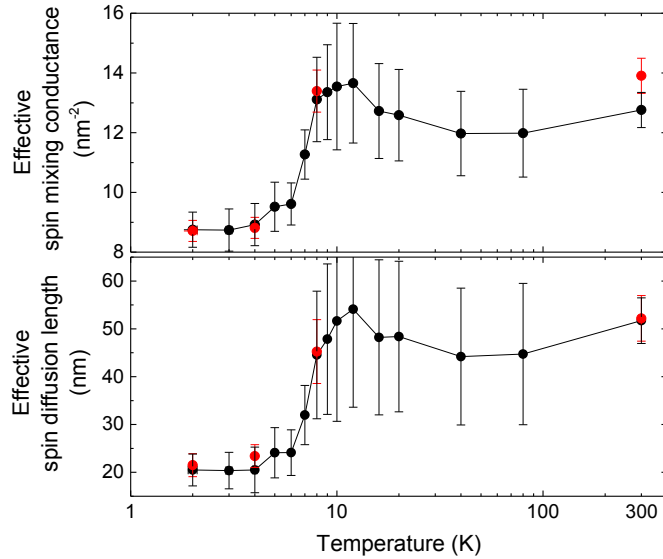
We estimate here two essential parameters of the effective spin mixing conductance (real part)  $g_r^{\uparrow\downarrow}$  and the effective spin diffusion length  $l_{sd}^{SC}$  that govern spin transport properties. For a given  $f$ , the  $t_{Nb}$  dependence of  $\mu_0\Delta H$  (Fig. 2b, main text) can be described by the following equation<sup>3,4,S6,S7</sup>:

$$\mu_0\Delta H(t_{SC}) \approx \frac{4\pi f}{\sqrt{3}\gamma} \cdot [\alpha_0 + \alpha_{sp}(t_{SC})], \quad (S4)$$

$$\alpha_{sp}(t_{SC}) = 2 \cdot \left( \frac{g_L \mu_B g_r^{\uparrow\downarrow}}{4\pi M_s t_{FM}} \right) \cdot \left[ 1 + \frac{g_r^{\uparrow\downarrow} \mathcal{R}_{SC}}{\tanh\left(\frac{t_{SC}}{l_{sd}^{SC}}\right)} \right]^{-1}, \quad (S5)$$

where  $\mathcal{R}_{SC} \equiv \rho_{SC} l_{sd}^{SC} e^2 / 2\pi\hbar$ ,  $\rho_{SC}$  is the resistivity of the Nb ( $7 - 8 \mu\Omega\text{-cm}$  for  $T_c \leq T \leq 80$  K,  $15 \mu\Omega\text{-cm}$  at 300 K, see Fig. S6), and  $e$  is the electron charge. The  $\rho_{SC}$  value for  $T_c < T$  was determined using the quasi-particle (QP) resistivity  $\sim \rho_0 / [2f_0(\Delta)]$ ,<sup>14</sup> where  $\rho_0$  is the residue resistivity of the Nb immediately above  $T_c$  ( $7 - 8 \mu\Omega\text{-cm}$ ) and  $f_0(\Delta) = [\exp(\Delta/k_B T) + 1]^{-1}$  is the Fermi-Dirac distribution function at the (effective)

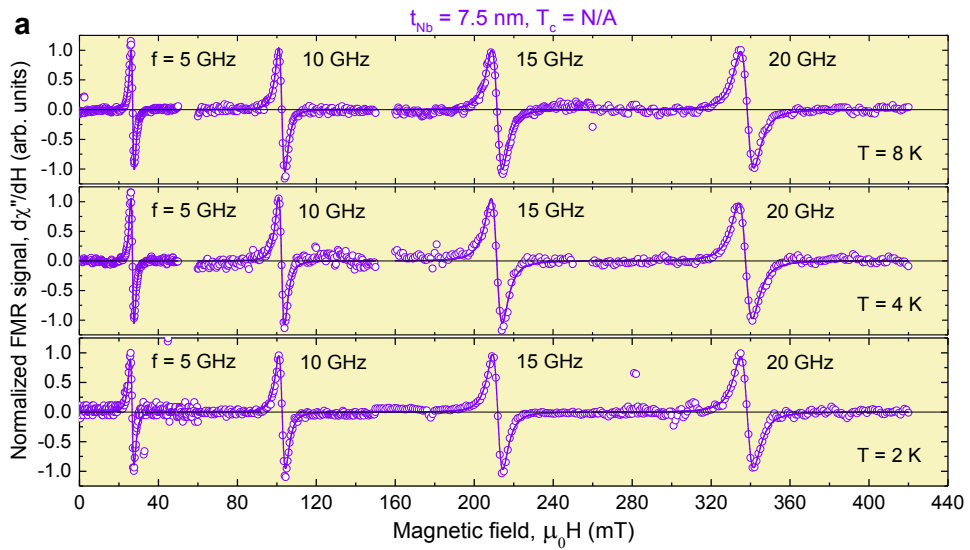
superconducting gap  $\Delta$  of the Nb (Sec. S10). In calculating  $f_0(\Delta)$  because of the (inverse) proximity effect, we assumed that  $\Delta$  is of spatial dependence as  $\Delta(z) = \Delta_0 \cdot (z/\xi_{sc})$  for  $0 \leq z \leq \xi_{sc}$  whereas  $\Delta(z) = \Delta_0$  for  $\xi_{sc} < z \leq t_{sc}$ , where  $\Delta_0$  is the superconducting gap of bare Nb films (see Sec. S9) and  $\xi_{sc}$  is the superconducting coherence length.  $t_{FM}$  and  $t_{SC}$  are the  $\text{Ni}_{80}\text{Fe}_{20}$  thickness (6 nm) and the Nb thickness (7.5 – 60 nm), respectively.  $M_s$  is the saturation magnetization of the  $\text{Ni}_{80}\text{Fe}_{20}$  (756 kA/m for  $T \leq 80$  K, 684 kA/m at 300 K). Note that the prefactor 2 takes into account the spin pumping through double interfaces. Since, for the samples used here, the contribution of  $\mu_0\Delta H_0$  in Eq. (S3) was found to be negligible ( $< |0.5 \text{ mT}|$ , see Fig. S4), we can use Eq. (S4) to evaluate the spin transport parameters. From the estimated values of  $g_r^{\uparrow\downarrow}$  and  $l_{sd}^{SC}$  (Fig. S3), it can be seen that in the superconducting state, the spin injection efficiency is reduced by about 25% and the spin transport length drops to approximately half of that ( $\sim 50$  nm) in the normal state.

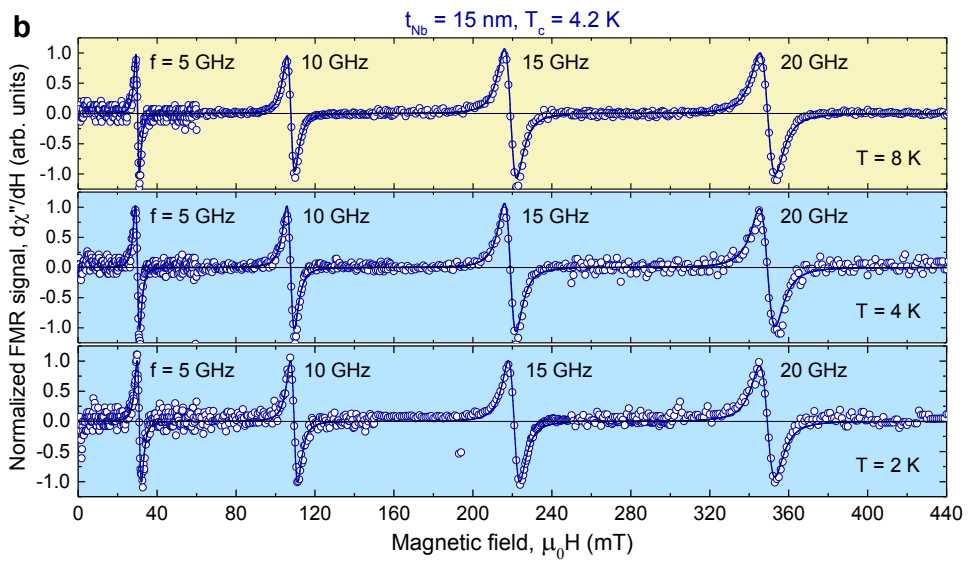


**Figure S3.** Temperature dependence of effective spin mixing conductance and effective spin diffusion length, estimated from Fig. 2b (main text) using Eqs. (S4) and (S5). For comparison, the spin transport parameters calculated based on the  $t_{\text{Nb}}$  dependence of  $\alpha$  (see Sec. S4) are also presented by the red symbols. Error bars denote standard deviation of fitting.

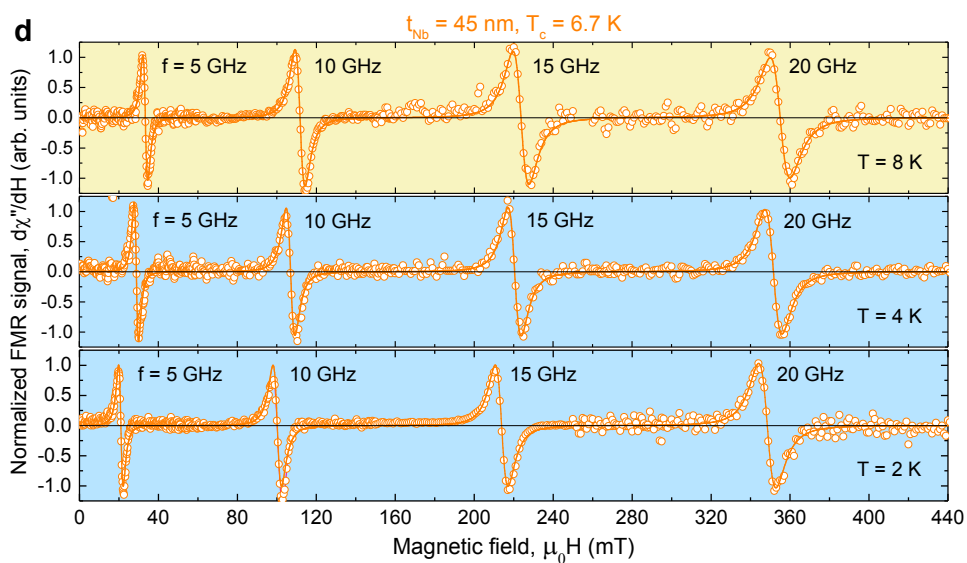
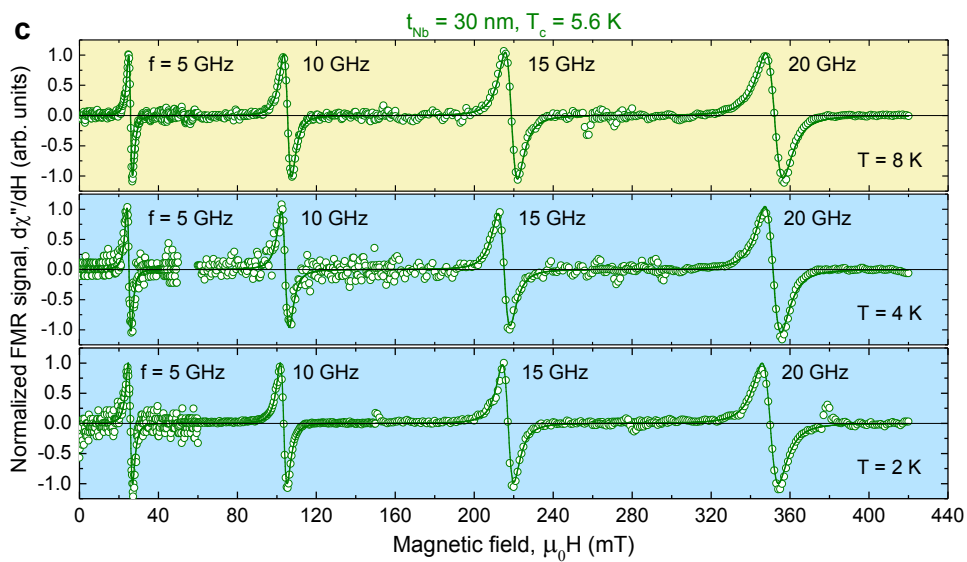
**Section S4. MW frequency dependence of FMR spectra for Nb/Ni<sub>80</sub>Fe<sub>20</sub>/Nb samples at low temperatures.**

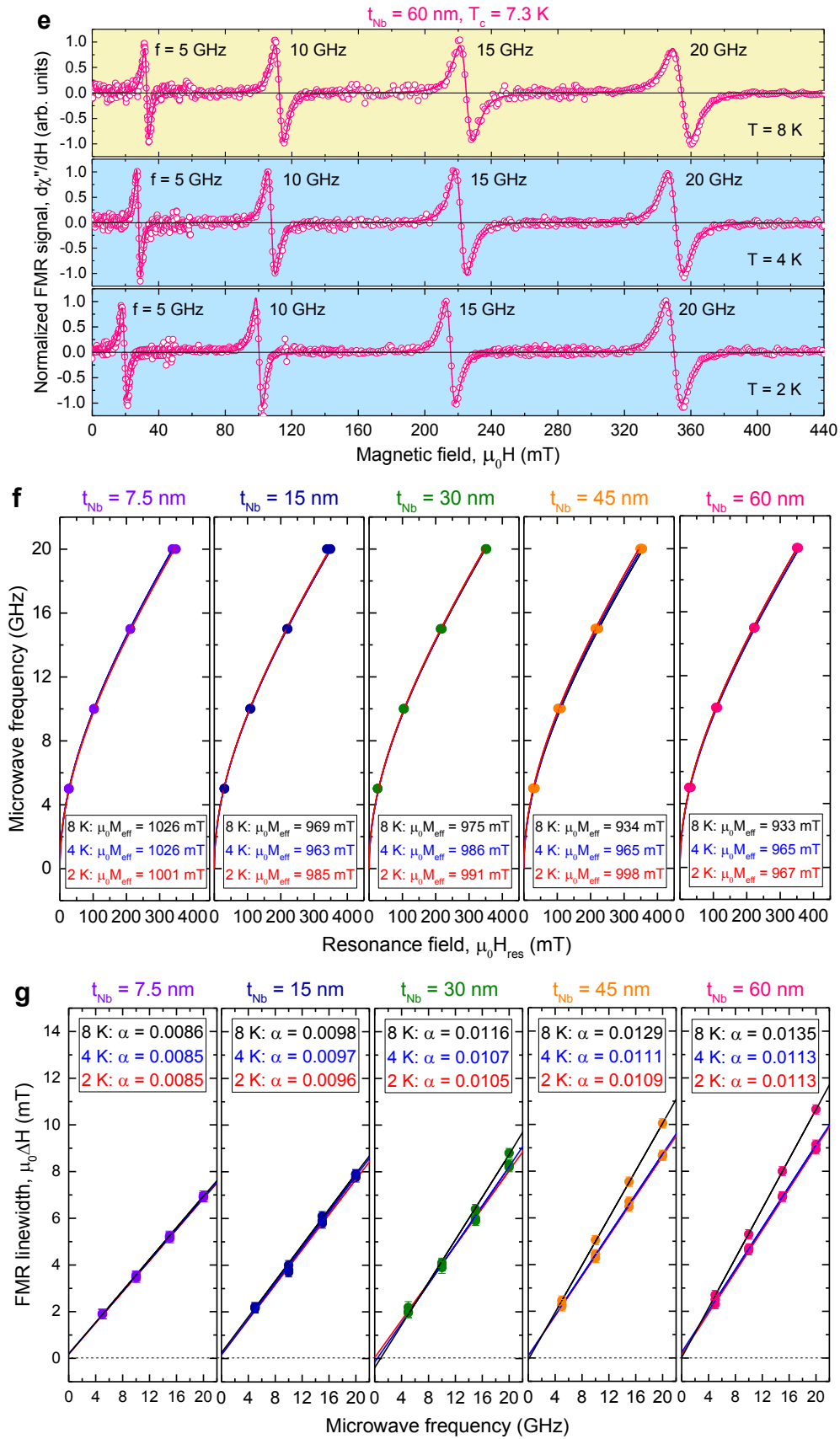
It was shown in Sec. S3 that the superconducting correlation can be responsible for the suppressed spin transport properties by analyzing the temperature  $T$  dependence of FMR linewidth at the fixed  $f$  of 20 GHz (see Fig. 2b, main text). In this section, we further confirm that based on the  $f$  dependence of FMR spectra, the noticeable reduction of Gilbert damping  $\alpha$  indeed happens across the superconducting transition  $T_c$ . Figures S4a-S4e show the entire set of the  $f$  dependence of FMR spectra for the samples without Pt layers measured at low  $T$  of 2, 4, and 8 K. This enables us to calculate  $\mu_0 M_{\text{eff}}$  (Fig. S4f) and  $\alpha$  (Fig. S4g) for each  $t_{\text{Nb}}$  using Eqs. (S2) and (S3), respectively. As summarized in Figs. S4h and S4i, it is evident that whereas  $\mu_0 M_{\text{eff}}$  varies weakly with  $t_{\text{Nb}}$  (regardless of  $T$ ),  $\alpha$  is of considerable dependence on  $t_{\text{Nb}}$  and the reduction of  $\alpha$  across  $T_c$  (from 8 K down to 2 K) gets more pronounced when the Nb is thicker. We also note that the  $t_{\text{Nb}}$  dependence of  $\alpha$  is well described by the spin pumping theory (Fig. S4i, solid lines), and the corresponding spin transport parameters (see Fig. S3, red symbols) clarify again that the suppressed flow of spin currents below  $T_c$  is caused by the superconducting correlation.





c





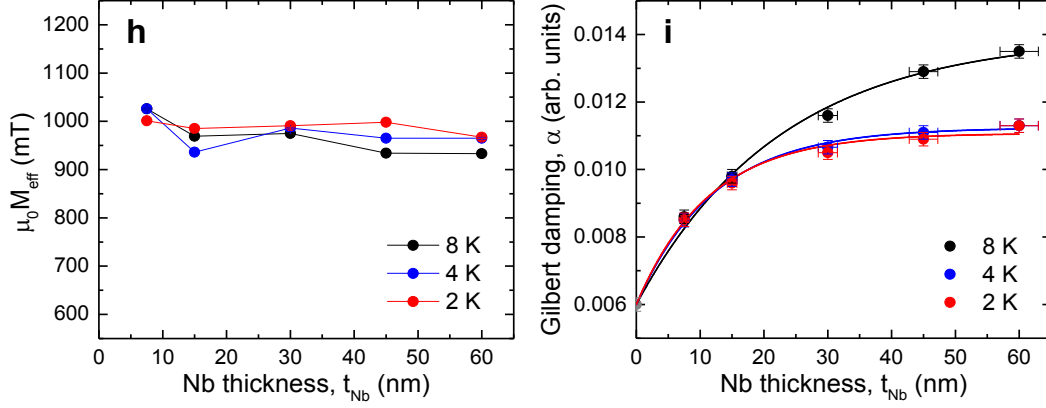
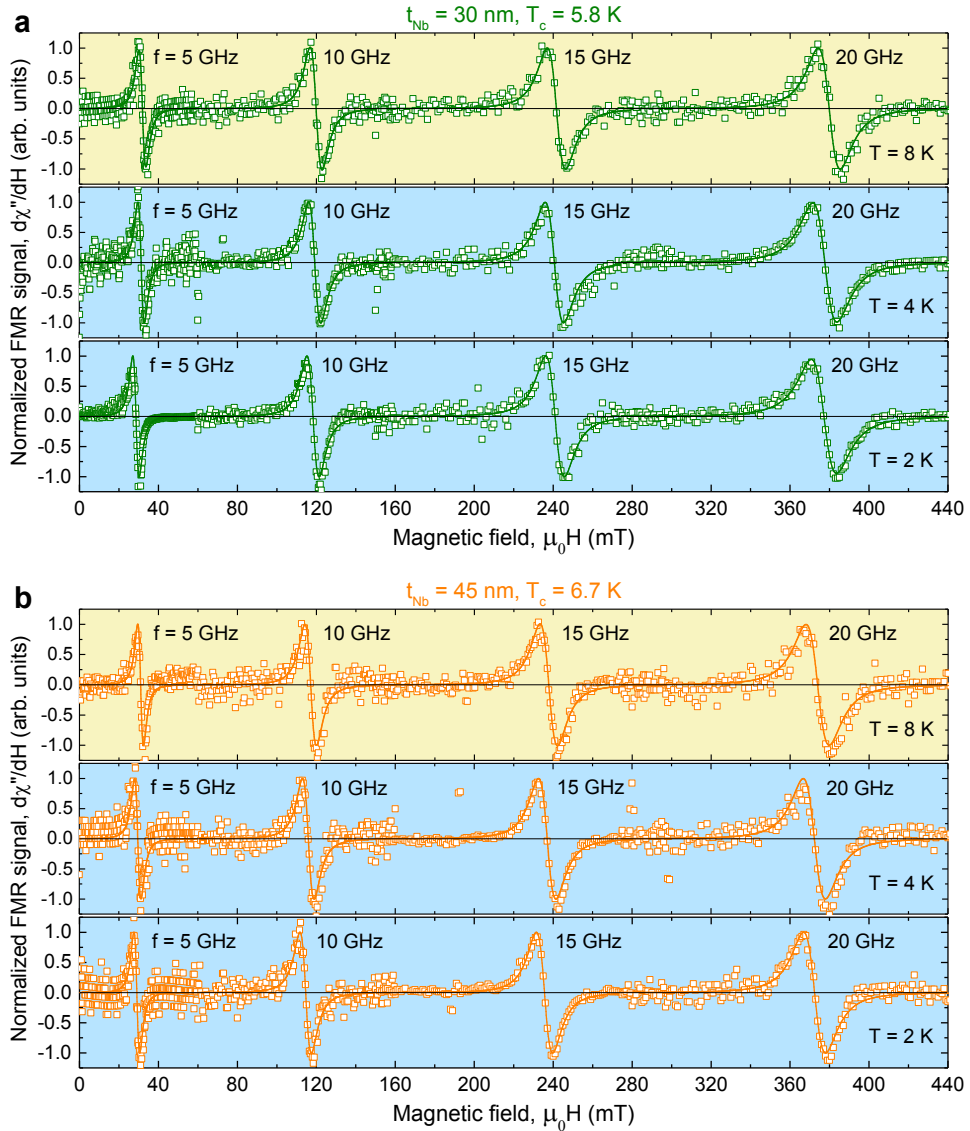


**Figure S4. MW frequency dependence of FMR spectra for the Nb/Ni<sub>80</sub>Fe<sub>20</sub>/Nb samples at 2, 4, and 8 K.** Representative set of FMR spectra for Nb/Ni<sub>80</sub>Fe<sub>20</sub>/Nb samples with different Nb thicknesses  $t_{\text{Nb}}$  of 7.5, 15, 30, 45, and 60 nm for **a-e**, respectively, taken at the temperature  $T$  of 2, 4, and 8 K (from bottom to top) with the microwave frequency  $f$  of 5, 10, 15, and 20 GHz (from left to right). The yellow (blue) background represents the normal (superconducting) state of Nb. Note that the 7.5 nm thick Nb does not show the superconducting transition down to 2 K. **f**, Microwave frequency vs. resonance magnetic field  $\mu_0 H_{\text{res}}$ . The solid lines are fits to extract the effective saturation magnetization  $\mu_0 M_{\text{eff}}$  via Kittel's formula [Eq. (S2)]. **g**, FMR linewidth  $\mu_0 \Delta H$  as a function of microwave frequency  $f$ . The solid lines are fitting curves to deduce the Gilbert damping constant  $\alpha$  using Eq. (S3) of the main text. Note also that in any case, the zero-frequency line broadening  $\mu_0 \Delta H_0$  is less than [0.5 mT]. **h**, Summary of  $\mu_0 M_{\text{eff}}$  as a function of  $t_{\text{Nb}}$ . **i**, Summary of Gilbert damping constant  $\alpha$  as a function of  $t_{\text{Nb}}$ . The solid lines are fits to estimate the effective values of spin mixing conductance and spin diffusion length using the spin pumping model [Eq. (S5)], which were presented in Fig. S3 (red symbol). Error bars denote standard deviation of multiple measurements.

### **Section S5. MW frequency dependence of FMR spectra for Pt/Nb/Ni<sub>80</sub>Fe<sub>20</sub>/Nb/Pt samples at low temperatures.**

As in Sec. S4, we here assure that from the analysis on FMR spectra as a function of  $f$  taken around  $T_c$  (Figs. S5a-S5d), the remarkable enhancement of  $\alpha$  can occur even in the superconducting state when attached to a strong spin-orbit coupled material (Pt). Figures S4e and S4f respectively summarize the extracted  $\mu_0 M_{\text{eff}}$  and  $\alpha$  values from the low  $T$  data

on two different  $t_{\text{Nb}}$  of 30 and 45 nm, where the former (latter) is thinner (thicker) than  $2\zeta_{\text{sc}}$  [here  $\zeta_{\text{sc}}$  is the superconducting coherence length in the dirty limit ( $\sim 16$  nm at 2 K) and the prefactor 2 considers two interfaces at opposite sides of the Nb layer]. It is worth noting that in contrast with the weak  $T$  dependence of  $\mu_0 M_{\text{eff}}$  (Fig. S5e),  $\alpha$  clearly reveals the distinctive behavior with decreasing  $T$  (Fig. S5f). For  $t_{\text{Nb}} = 30$  nm ( $< 2\zeta_{\text{sc}}$ ), the large enhancement of  $\alpha$  is visible at low  $T$  while for  $t_{\text{Nb}} = 45$  nm ( $> 2\zeta_{\text{sc}}$ ),  $\alpha$  is suppressed across  $T_c$ , as in the case without Pt layers (see Fig. S4i). This result strongly supports the finding that the superconductivity in concert with the spin-orbit coupling (SOC) for the intermediate  $t_{\text{Nb}}$  leads to the enhanced magnetization damping and thereby the increased flow of spin currents.



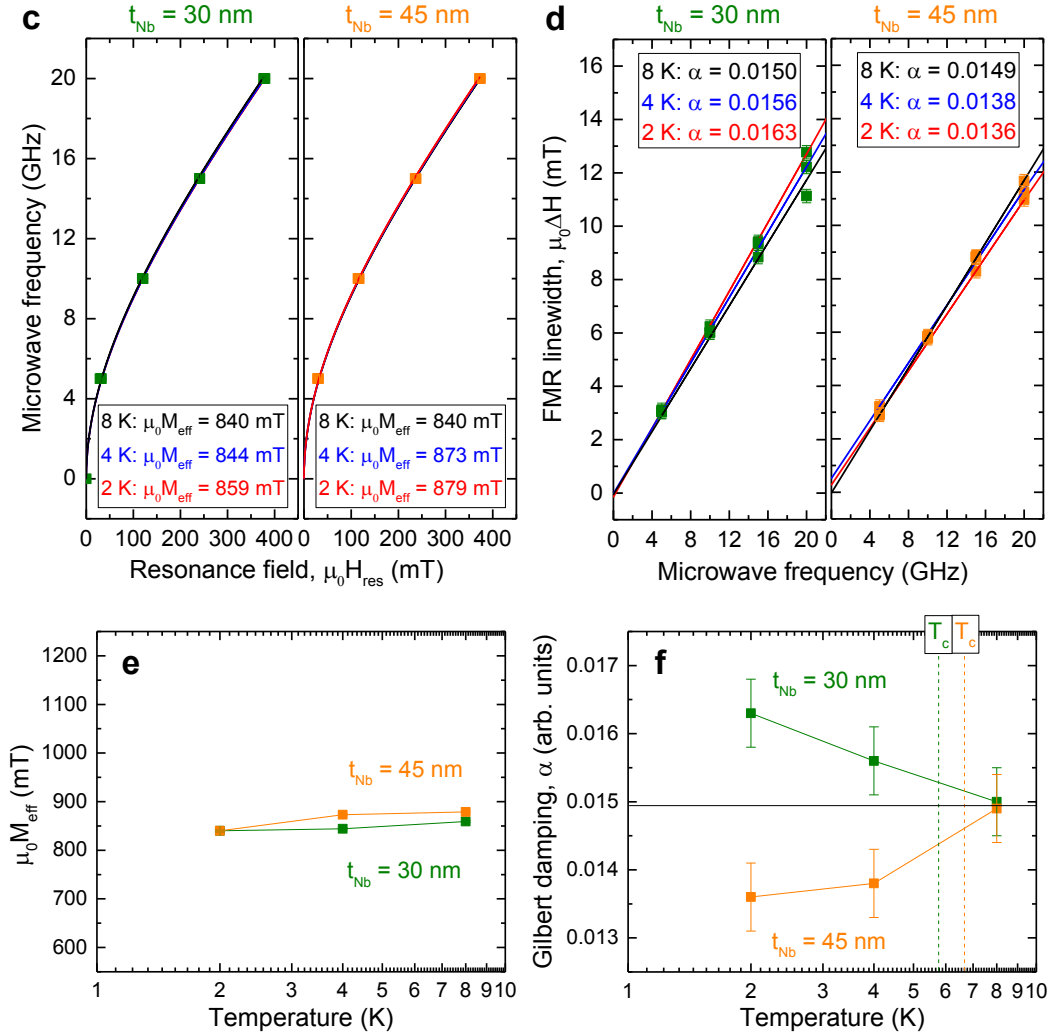


**Figure S5. MW frequency dependence of FMR spectra for the Pt/Nb/Ni<sub>80</sub>Fe<sub>20</sub>/Nb/Pt samples at 2, 4, and 8 K.** a-d, The data shown are similar to those in Fig. S3 but now for the samples of  $t_{\text{Nb}} = 30$  and 45 nm with Pt layers. Note that for both cases, the zero-frequency line broadening  $\mu_0 \Delta H_0$  is smaller than  $|0.5 \text{ mT}|$ . The yellow (blue) background represents the normal (superconducting) state of Nb. Summary of the effective saturation magnetization  $\mu_0 M_{\text{eff}}$  and Gilbert damping constant  $\alpha$  in the low temperature  $T$  range of 2–8 K for e-f, respectively. The dashed lines indicate the superconducting transition temperature  $T_c$  and the black solid line is the average value of  $\alpha$  in the normal state. Error bars denote standard deviation of multiple measurements.

**Section S6. Influence of the thickness-dependent resistivity of Nb films on spin transport parameter.**

In this section, we investigate how the thickness-dependent resistivity  $\rho$  of Nb films affects the estimation of spin diffusion length  $l_{sd}$  using Eq. (S5), where the thickness-independent  $\rho$  is assumed. As recently pointed out<sup>S8,S9</sup>, for a more precise estimation of  $l_{sd}$ , one should take into account the thickness dependence of  $\rho$  of the spin sink layer. Such consideration become particularly important when  $l_{sd}$  is comparable to the mean free path  $l_{mfp}$  or shorter, for which the surface scattering mechanism is dominant and so the significant thickness dependence of  $\rho$  is expected.

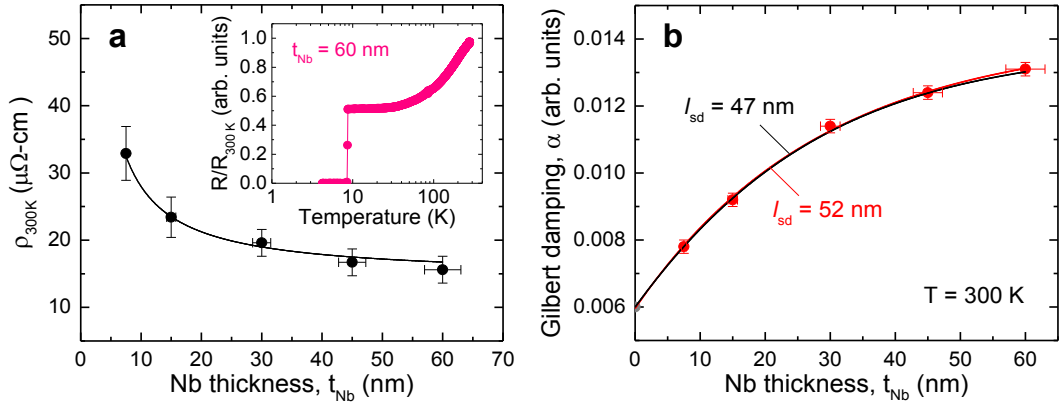


**Figure S6. Thickness dependence of resistivity on Nb films.** **a**, Resistivity  $\rho$  of Nb films on SiO<sub>2</sub>(250 nm)/Si substrates as a function of thickness ( $t_{Nb}$ ) at 300 K. The black line is the fitting curve using Eq. (S6). The inset shows the normalized resistance  $R/R_{300\text{ K}}$  vs. temperature  $T$  plot for the 60-nm-thick Nb film. **b**, Gilbert damping constant  $\alpha$  as a function of  $t_{Nb}$ , which was presented in the inset of Fig. 2B (main text). The black line is a fit taking into account the  $t_{Nb}$  dependence of  $\rho$  (from Fig. S6a) while the red line is a fit assuming the constant (bulk-like)  $\rho$  of the 60-nm-thick Nb film. Error bars denote standard deviation of multiple measurements.

Figure S6A shows the measured  $\rho$  of Nb films, for  $7.5 \leq t_{Nb} \leq 60$  nm, using the four-point method either on the perimeter of the film (van der Pauw geometry<sup>S10</sup>) or the trace of the mirror place (collinear geometry<sup>S11</sup>). The thickness dependence of  $\rho_{Nb}$  can be empirically described by:

$$\rho_{Nb}(t_{Nb}) = \rho_b + \frac{\rho_s}{t_{Nb}}, \quad (\text{S6})$$

where  $\rho_b$  is the bulk resistivity of the Nb ( $15 \mu\Omega\text{-cm}$  at 300 K) and  $\rho_s$  is the surface

resistivity coefficient ( $1.4 \times 10^{-5} \mu\Omega\text{-cm}^2$ ). The observed small deviation of  $\rho_{Nb}$  from the bulk value (Fig. S5a) is consistent with what is expected in the thickness regime over  $l_{mfp}$  [3 (6) nm for Nb at 300 (10) K]<sup>33</sup>. Here  $l_{mfp}$  of the Nb is determined from  $l_{mfp} \cdot \rho_{Nb} = 3.7 \text{ p}\Omega\text{-cm}^2$ . Owing to the small deviation, the extracted value of  $l_{sd}$  (47 nm) from Gilbert damping  $\alpha$  as a function of  $t_{Nb}$  with a fit considering the thickness-dependent  $\rho_{Nb}$  (Fig. S6b, red line) was found to be more or less similar to that (52 nm) with a fit assuming the constant (bulk-like)  $\rho_{Nb}$  (Fig. S6b, black line). We can conclude that for our samples ( $t_{Nb} \geq l_{mfp}$ ), the model assuming constant  $\rho_{Nb}$  mostly captures the  $t_{Nb}$  dependence of  $\alpha$  (or FMR linewidth) and yields the reliable value of  $l_{sd}$ .

### **Section S7. Quantification of the suppressed spin current density (without Pt) in the superconducting state.**

Using the standard spin pumping theory<sup>3,4,S6,S7</sup>, we here quantify how much the pumped spin current density in the Nb(60 nm)/Ni<sub>80</sub>Fe<sub>20</sub>(6 nm)/Nb(60 nm) sample is reduced due to the presence of the superconducting gap  $2\Delta$ . The (pumped) spin current density  $j_s^0$  at each Ni<sub>80</sub>Fe<sub>20</sub>/Nb interface is given by<sup>3,4,S6,S7</sup>:

$$j_s^0 = \left(\frac{\hbar\omega}{4\pi}\right) \cdot G_r^{\uparrow\downarrow} \cdot (\sin \theta_c)^2 \cdot \left[ 2\omega \cdot \left( \frac{\mu_0 M_{eff}\gamma + \sqrt{(\mu_0 M_{eff}\gamma)^2 + (2\omega)^2}}{(\mu_0 M_{eff}\gamma)^2 + (2\omega)^2} \right) \right] \cdot \left(\frac{2e}{\hbar}\right), \quad (\text{S7})$$

$$\sin \theta_c = \frac{\mu_0 h_{rf}\gamma}{\alpha} \cdot \sqrt{\frac{\mu_0 M_{eff}\gamma + \sqrt{(\mu_0 M_{eff}\gamma)^2 + (2\omega)^2}}{(\mu_0 M_{eff}\gamma)^2 + (2\omega)^2}}, \quad (\text{S8})$$

where  $\omega = 2\pi f$  is the angular frequency,  $G_r^{\uparrow\downarrow} \equiv g_r^{\uparrow\downarrow} \cdot \left[ 1 + g_r^{\uparrow\downarrow} \mathcal{R}_{SC} / \tanh\left(\frac{t_{SC}}{l_{sd}}\right) \right]^{-1}$ ,  $\theta_c$  is the magnetization precession angle, and  $\mu_0 h_{rf}$  is the amplitude of MW magnetic field ( $\sim 0.1$  mT). Using the extracted values of  $g_r^{\uparrow\downarrow}$  (see Fig. S3),  $\alpha$  (Fig. S4g), and  $\mu_0 M_{eff}$  (Fig. S4f), we calculated  $j_s^0$  as a function of MW frequency  $f$  at  $T = 2, 4$ , and 8 K (Fig. S7a). Note that  $j_s^0$  gradually decreases with increasing  $f$  due to the decreased  $\theta_c$  at a high  $f$ <sup>S12</sup>, as shown in the set of Fig. S7a. The normalized  $j_s^0$  vs.  $T$  plot in Fig. S7b shows that  $j_s^0$  in the superconducting state ( $T = 2$  and 4 K) is reduced by about 30% compared with that in the normal state ( $T = 8$  K), almost regardless of  $f$ .

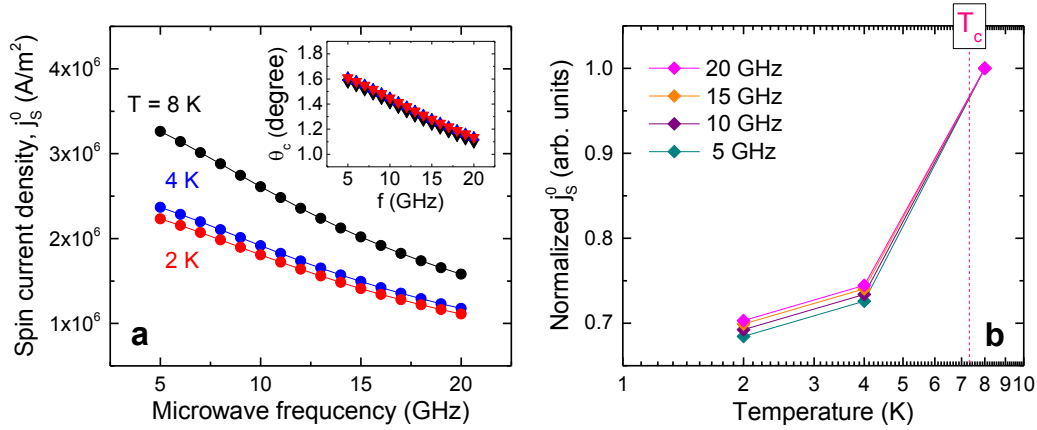


**Figure S7. Pumped spin current density in the Nb(60 nm)/Ni<sub>80</sub>Fe<sub>20</sub>(6 nm)/Nb(60 nm) sample.** **a**, Spin current density  $j_s^0$  at the Ni<sub>80</sub>Fe<sub>20</sub>/Nb interface as a function of microwave frequency  $f$ , calculated using Eqs. (S7) and (S8). The inset shows the associated precession angle  $\theta_c$  as a function of  $f$ . **b**, Normalized  $j_s^0$  in the low temperatures  $T$  range of 2–8 K for various  $f$ .

For instructive purpose, we also calculated the steady state value of spin accumulation  $\Delta\mu^0$  at the Nb interface, which is determined by balancing the net amount of injected spins with the amount of spin flips in the Nb per unit time, which can be expressed in terms of a material parameter, namely the spin resistance  $r_{SC} \equiv \rho_{SC} l_{sd}^{SC}$ , of the Nb,

$$\Delta\mu^0 = (2e) \cdot r_{SC} \cdot j_s^0, \quad (\text{S9})$$

where the value of  $r_{SC}$  controls the conversion of  $j_s^0$  into  $\Delta\mu^0$ . Using the deduced values of  $r_{SC} = 0.2\text{--}0.3 \text{ } \Omega\text{-}\mu\text{m}^2$  (see Fig. S3) and  $j_s^0 = 1\text{--}2 \times 10^6 \text{ A/m}^2$  (Fig. S7a), we determined  $\Delta\mu^0 = 0.4\text{--}1.2 \text{ } \mu\text{eV}$  at  $f = 20 \text{ GHz}$  for  $T \leq 8 \text{ K}$ .

### **Section S8. FMR linewidth & resonance field vs. normalized temperature $T/T_c$ .**

The overall summary of FMR linewidth  $\mu_0\Delta H$  (resonance field  $\mu_0 H_{\text{res}}$ ) as a function of  $T/T_c$  for the samples with and without Pt layers is shown in Fig. S8a (Fig. S8b). This clarifies that the interplay of the superconductivity and SOC markedly alters the transport/dissipation characteristics of spin-polarized currents.

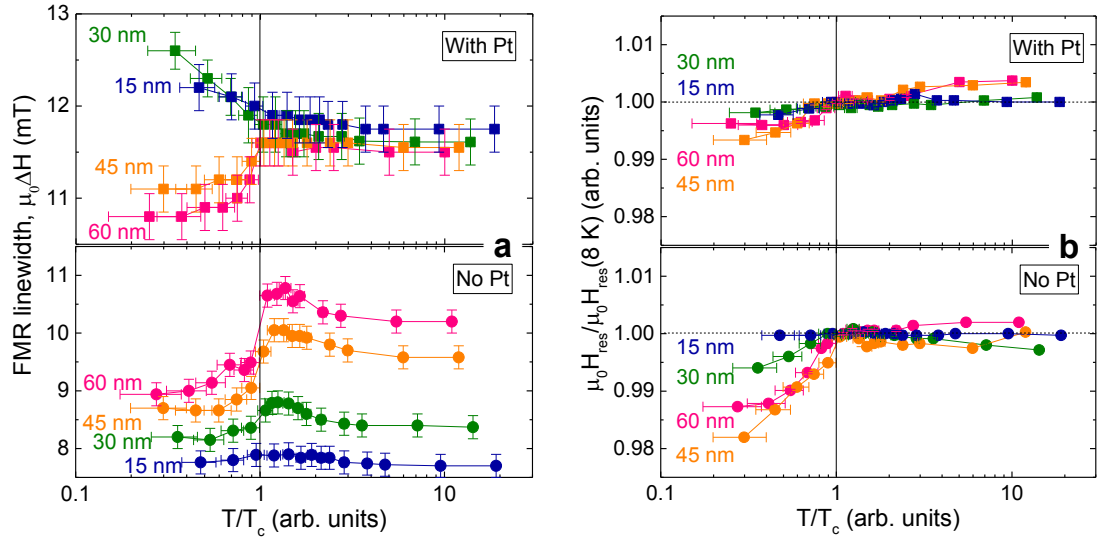


**Figure S8. FMR linewidth and resonance field as a function of normalized temperature  $T/T_c$ .** **a**, Top and bottom panels are respectively from the data (FMR linewidth  $\mu_0\Delta H$ ) of the samples with and without Pt layers, which were displayed in the main text but now as a function of  $T/T_c$ . **b**, The data shown are similar to Fig. S8a but now for the normalized resonance field  $\mu_0 H_{res}/\mu_0 H_{res}(8\text{ K})$ . Error bars denote standard deviation of multiple measurements.

**Section S9. Superconducting transition temperature  $T_c$  for various sample structures.**

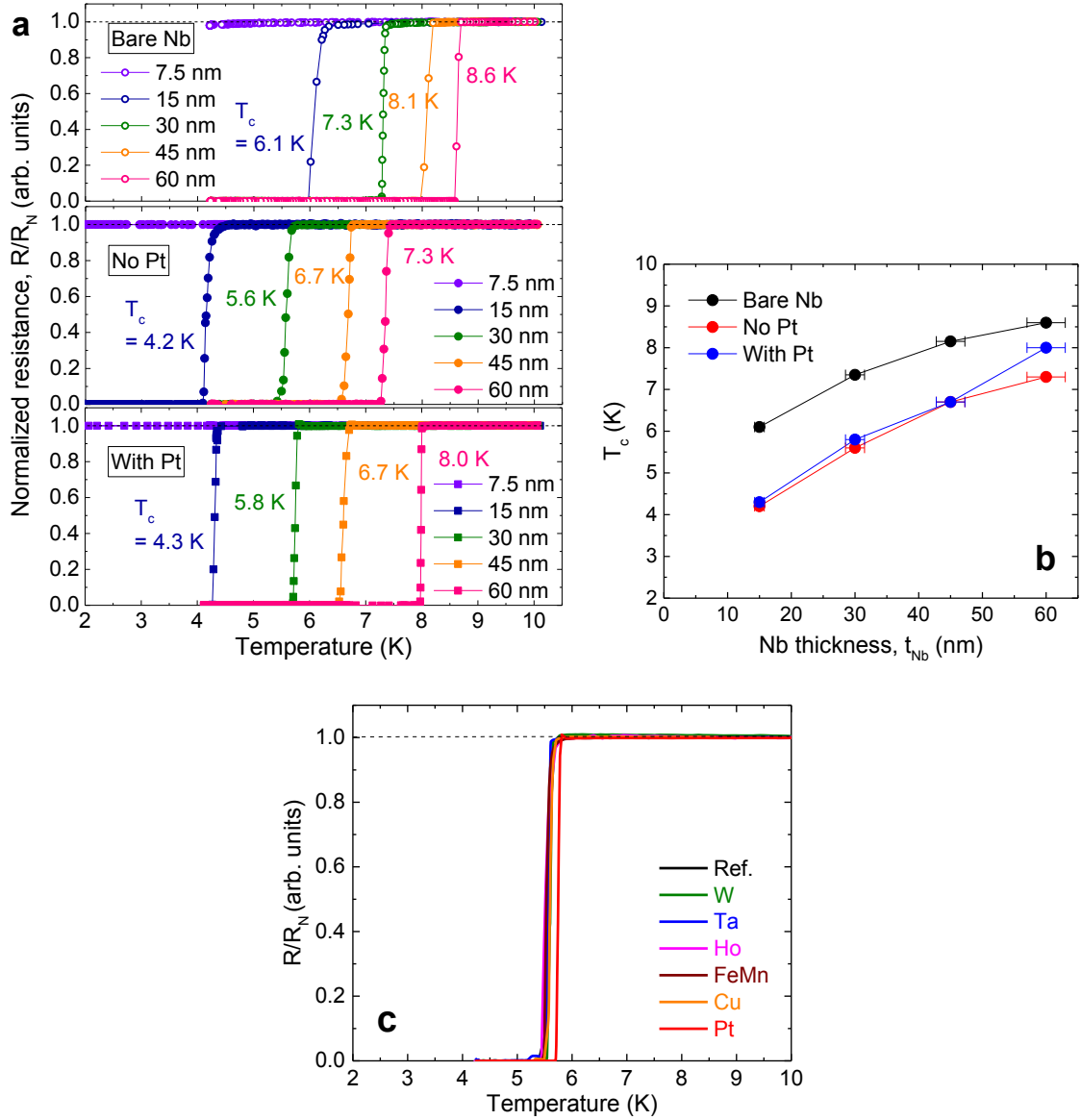


**Figure S9. Normalized resistance  $R/R_N$  vs. temperature  $T$  plots for various sample structures.** The data are shown for **a**, Bare Nb( $t_{Nb}$ ) films with their thickness  $t_{Nb}$  of 7.5–60 nm (top); Nb( $t_{Nb}$ )/Ni<sub>80</sub>Fe<sub>20</sub>(6 nm)/Nb( $t_{Nb}$ ) samples with  $t_{Nb} = 7.5$ –60 nm (middle); Pt(5 nm)/Nb( $t_{Nb}$ )/Ni<sub>80</sub>Fe<sub>20</sub>(6 nm)/Nb( $t_{Nb}$ )/Pt(5 nm) with  $t_{Nb} = 7.5$ –60 nm (bottom); **b**, Summary of  $t_{Nb}$  dependence of  $T_c$ ; **c**, Nb(30 nm)/Ni<sub>80</sub>Fe<sub>20</sub>(6 nm)/Nb(30 nm) sandwiched by various spin-sink materials. Error bars denote standard deviation of multiple measurements.

The full set of  $T_c$  curves for several sample structures are presented in Fig. S9. In Fig. S9b, we can see that  $T_c$  suppression is dominant at the Ni<sub>80</sub>Fe<sub>20</sub>/Nb interface, as expected

for the (inverse) proximity effect of Ni<sub>80</sub>Fe<sub>20</sub>.

### **Section S10. Superconducting energy gap & critical magnetic field vs. temperature.**

Using the measured values of  $T_c$  from our samples (see Sec. 9), we estimated the (Bardeen–Cooper–Schrieffer type) temperature  $T$  dependence of the superconducting energy gap  $2\Delta$  (Fig. S10a and S10b) and the (in-plane upper) critical magnetic field  $\mu_0 H_{c2\parallel}$  (Fig. S10c and S10d) for each Nb layer:

$$\Delta(T) \approx 1.76k_B T_c \cdot \tanh \left[ 1.74 \sqrt{\frac{T}{T_c} - 1} \right], \quad (\text{S10})$$

$$\mu_0 H_{c2\parallel}(T) = \frac{\phi_0}{2\pi[\xi(0)]^2} \cdot \left( 1 - \left( \frac{T}{T_c} \right)^2 \right), \quad (\text{S11})$$

where  $k_B$  is Boltzmann's constant,  $\phi_0$  is the flux quantum ( $2.07 \times 10^{-15} \text{ T} \cdot \text{m}^2$ ), and  $\xi(0)$  is the zero-temperature coherence length of Nb (7–13 nm)<sup>16,33</sup> in the dirty limit. We note in Fig. S10 that for all the superconducting Nb layers (15–60 nm) at low  $T$  (2–3 K), the energy interval of QP Fermi-Dirac distribution (order of  $k_B T$ ) is far below  $2\Delta$  and the magnitude ( $\leq 0.38 \text{ T}$ ) of dc magnetic fields applied for FMR is much weaker than  $\mu_0 H_{c2\parallel}$ . Note that the calculated  $\mu_0 H_{c2\parallel}(T)$  is consistent with those experimentally measured from sputter-grown Nb/Ni<sub>80</sub>Fe<sub>20</sub>/Nb films<sup>S13</sup>.

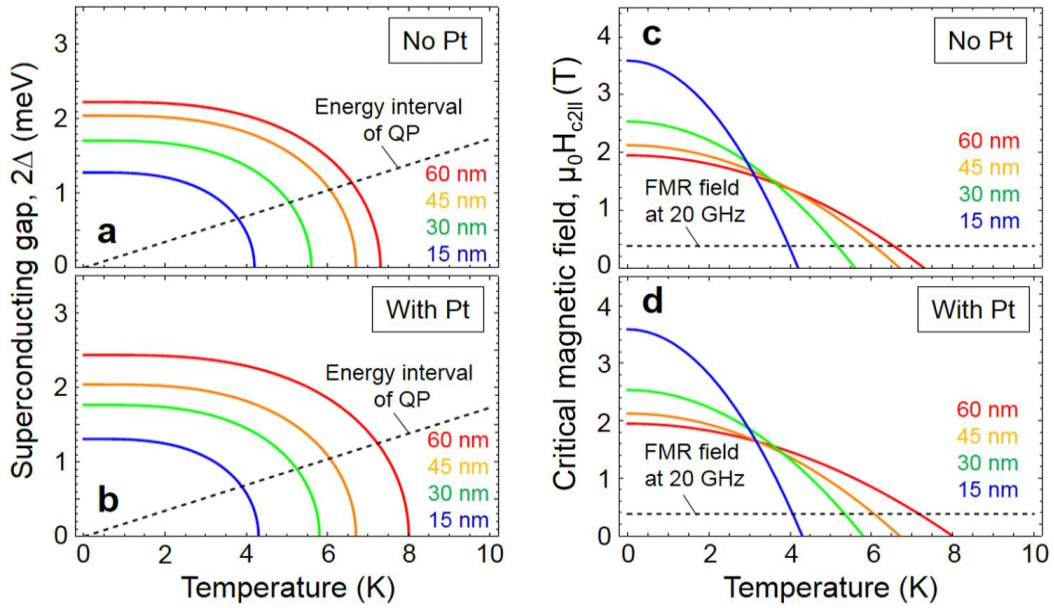


**Figure S10. Superconducting energy gap  $2\Delta$  and critical magnetic field  $\mu_0 H_{c2\parallel}$  as a function of temperature  $T$ . a,  $2\Delta(T)$  and c,  $\mu_0 H_{c2\parallel}(T)$  for Nb( $t_{\text{Nb}}$ )/Ni<sub>80</sub>Fe<sub>20</sub>(6**

nm)/Nb( $t_{\text{Nb}}$ ) samples with  $t_{\text{Nb}} = 15\text{--}60$  nm. **b**,  $2\Delta(T)$  and **d**,  $\mu_0 H_{c2\parallel}(T)$  for Pt(5 nm)/Nb( $t_{\text{Nb}}$ )/Ni<sub>80</sub>Fe<sub>20</sub>(6 nm)/Nb( $t_{\text{Nb}}$ )/Pt(5 nm) with  $t_{\text{Nb}} = 15\text{--}60$  nm.

### **Section S11. Effect of MW power on the superconductivity of Nb.**

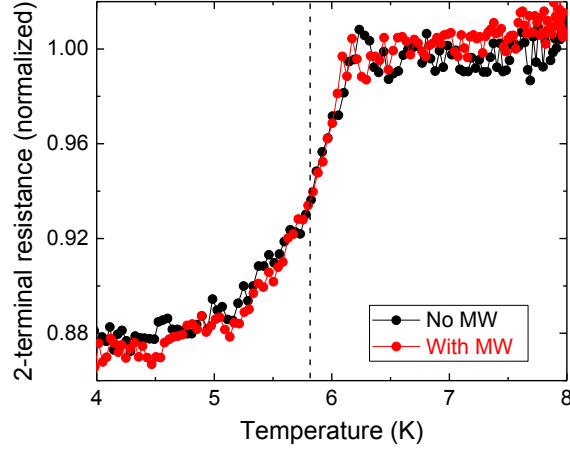


**Figure S11. Normalized 2-terminal resistance vs. temperature  $T$  plots with and without MW excitation.** The MW power was set to 10 dBm, as in FMR study, for this measurement. The dashed line represents the  $T_c$  value ( $\sim 5.8$  K) attained from the same sample in a (separate) liquid helium dewar with a four-point current-voltage method.

To investigate the effect of MW power on the superconductivity of Nb in terms of (unintentional) heating, we measured  $T_c$  curves for a Pt(5 nm)/Nb(30 nm)/Ni<sub>80</sub>Fe<sub>20</sub>(6 nm)/Nb(30 nm)/Pt(5 nm) sample with and without MW excitation. As shown in Fig. S11, it turns out that a few mW of (actual) MW power absorbed in the sample has no effect on  $T_c$  of the Nb layer.

Precessing Ni<sub>80</sub>Fe<sub>20</sub> can also be a heat source. The amount of heat generated from FMR is determined by the MW frequency  $f$  and the precession cone angle  $\theta_c$  (see Sec. S7) as  $\theta_c \cdot (hf)$ , where  $h$  is Planck's constant. For  $f = 20$  GHz, the expected heat generation is in the range of 0.01–0.02 K, more than two orders of magnitude smaller than the base temperature (2 - 300 K).

### **Section S12. Investigation of superconducting spin currents for other $t_{\text{Nb}}$ samples**

**with Pt.**

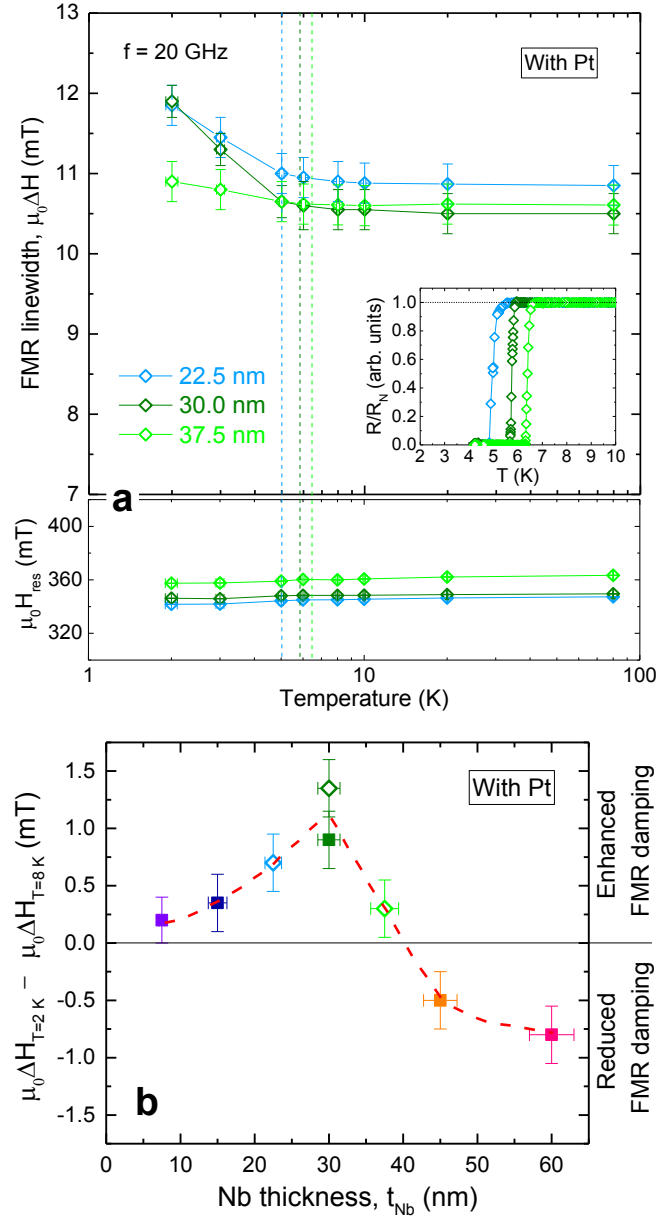


**Figure S12. Superconducting spin transport as a function of Nb thickness  $t_{\text{Nb}}$  for the samples with Pt. a,** Temperature  $T$  dependence of the FMR linewidth  $\mu_0\Delta H$  (top) and the resonance magnetic field  $\mu_0H_{\text{res}}$  (bottom) for  $t_{\text{Nb}} = 22.5, 30.0,$  and  $37.5$  nm. The dashed lines indicate the superconducting transition temperature  $T_c$  extracted from the normalized resistance  $R/R_N$  vs. temperature  $T$  plots [inset of Fig. S12a]. **b,** Overall summary of  $t_{\text{Nb}}$  dependence of the FMR linewidth difference across  $T_c$ , denoted as  $\mu_0\Delta H(2\text{ K}) - \mu_0\Delta H(8\text{ K})$ , which is also presented in the main text (Fig. 2d). The red dashed line is a guide to the eyes; the rectangular and diamond symbols represent two

independent sets of the samples grown each in a single deposition run. Error bars denote standard deviation of multiple measurements.

In order to investigate the superconducting spin transport as a function of Nb thickness  $t_{\text{Nb}}$  in detail, we have repeated the FMR measurements on a new set of Pt(5 nm)/Nb( $t_{\text{Nb}}$ )/Ni<sub>80</sub>Fe<sub>20</sub>(6 nm)/Nb( $t_{\text{Nb}}$ )/Pt(5 nm) samples with  $t_{\text{Nb}} = 22.5, 30.0, \text{ and } 37.5$  nm (Fig. S12a). *We note that for all these samples, a clear enhancement of the FMR linewidth  $\mu_0\Delta H$  and thereby the spin current flow (to the Pt layer) below  $T_c$  is visible.* For completeness, we have also plotted the  $t_{\text{Nb}}$  dependence of the FMR linewidth change across  $T_c$ , denoted as  $\mu_0\Delta H(2 \text{ K}) - \mu_0\Delta H(8 \text{ K})$ , for all the samples studied in Fig. S12b. Interestingly, we find that as  $t_{\text{Nb}}$  increases, the spin current flow is first enhanced until  $t_{\text{Nb}} = 30$  nm, and then it decays and becomes a negative (indicating the spin blocking) when  $t_{\text{Nb}} > 40$  nm. Qualitatively, this behaviour can be understood in the following manner.

In the samples with Pt, the magnitude of the superconducting spin transport via spin-triplet states in the Nb layers must be controlled by a tradeoff between i) the superconducting coherence length  $\xi_{\text{SC}}$  which determines the lengthscale over the triplet pairing penetrates from the interfaces and, ii) the spin-triplet pair density which should be proportional to the singlet superconducting energy gap  $\Delta$  (as the spin-triplet pair originates from the spin-singlet pair). When  $t_{\text{Nb}} \ll 2\xi_{\text{SC}}$  [recall that  $\xi_{\text{SC}}$  is the dirty-limit coherence length of the Nb ( $\sim 16$  nm at 2 K) and the prefactor 2 considers two interfaces at opposite sides of the Nb], the (converted) spin-triplet pair density is too low to induce large superconducting spin currents due to the low  $\Delta$  of a thin Nb layer. In contrast for  $t_{\text{Nb}} \gg 2\xi_{\text{SC}}$ , the induced triplet states do not bridge the thick Nb layer (with a high  $\Delta$ ) and so the spin transport channel is blocked.

## References

- S1. Celinski, Z., Urquhart, K. B. & Heinrich, B. Using ferromagnetic resonance to measure the magnetic moments of ultrathin films. *J. Magn. Magn. Mater.* **166**, 6–26 (1997).
- S2. Shaw, J. M., Nembach, H. T., Silva, T. J. & Boone, C. T. Precise determination of the

- spectroscopic g-factor by use of broadband ferromagnetic resonance spectroscopy. *J. Appl. Phys.* **114**, 243906 (2013).
- S3. Zhao Y. *et al.*, Experimental investigation of temperature-dependent Gilbert damping in permalloy thin films. *Sci. Rep.* **9**, 22890 (2016).
- S4. Heinrich, B. *Ultrathin Magnetic Structures*, Vol. III (Springer, Berlin, 2005).
- S5. Tserkovnyak, Y., Brataas, A. & Bauer, G. E. W. Enhanced Gilbert damping in thin ferromagnetic films. *Phys. Rev. Lett.* **88**, 117601 (2002).
- S6. Mizukami, S., Ando, Y. & Miyazaki, T. Effect of spin diffusion on Gilbert damping for a very thin permalloy layer in Cu/permalloy/Cu/Pt films. *Phys. Rev. B* **66**, 104413 (2002).
- S7. Tserkovnyak, Y., Brataas, A. & Bauer, G. E. W. Spin pumping and magnetization dynamics in metallic multilayers. *Phys. Rev. B* **66**, 224403 (2002).
- S8. Nguyen, M. -H., Ralph, D. C. & Buhrman, R. A. Spin torque study of the spin Hall conductivity and spin diffusion length in platinum thin films with varying resistivity. *Phys. Rev. Lett.* **116**, 126601 (2016).
- S9. Montoya E. *et al.* Spin transport in tantalum studied using magnetic single and double layers. *Phys. Rev. B* **94**, 054416 (2016).
- S10. van der Pauw, L. J. A Method of Measuring the Resistivity and Hall Coefficient on Lamellae. *Philips Tech. Rev.* **20**, 220–224 (1958).
- S11. Thorsteinsson, S. *et al.* Accurate microfour-point probe sheet resistance measurements on small samples. *Rev. Sci. Instrum.* **80**, 053902 (2009).
- S12. Gupta, S. *et al.* Important role of magnetization precession angle measurement in inverse spin Hall effect induced by spin pumping. *Appl. Phys. Lett.* **110**, 022404 (2017).
- S13. Cirillo1, C., Voltan, S., Ilyina, E. A., Hernández, J. M., García-Santiago, A., Aarts, A. & Attanasio, C. Long-range proximity effect in Nb-based heterostructures induced by a magnetically inhomogeneous permalloy layer. *New J. Phys.* **19**, 023037 (2017).